PHYSICAL REVIEW MATERIALS **6**, 074005 (2022)

Substrate influence on transition metal dichalcogenide monolayer exciton absorption linewidth broadening

Fuhui Shao,[1,2,3] Steffi Y. Woo,[1] Nianjheng Wu,[1,4] Robert Schneider,[5] Andrew J. Mayne,[4]
Steffen Michaelis de Vasconcellos,[5] Ashish Arora,[5,6] Benjamin J. Carey,[5] Johann A. Preuß,[5] Noémie Bonnet,[1]
Mauro Och,[7] Cecilia Mattevi,[7] Kenji Watanabe,[8] Takashi Taniguchi,[9] Zhichuan Niu,[2,3]
Rudolf Bratschitsch,[5] and Luiz H. G. Tizei[1,*]
[1]*Université Paris-Saclay, CNRS, Laboratoire de Physique des Solides, 91405 Orsay, France*
[2]*State Key Laboratory for Superlattices and Microstructures, Institute of Semiconductors, Chinese Academy of Sciences, Beijing 100083, China*
[3]*College of Materials Science and Opto-Electronic Technology, University of Chinese Academy of Sciences, Beijing 100083, China*
[4]*Université Paris-Saclay, CNRS, Institut des Sciences Moléculaires d'Orsay, 91405 Orsay, France*
[5]*Institute of Physics and Center for Nanotechnology, University of Münster, Wilhelm-Klemm-Straße 10, 48149 Münster, Germany*
[6]*Indian Institute of Science Education and Research, Dr. Homi Bhabha Road, 411008 Pune, India*
[7]*Department of Materials, Imperial College London, London SW7 2AZ, United Kingdom*
[8]*Research Center for Functional Materials, National Institute for Materials Science, 1-1 Namiki, Tsukuba 305-0044, Japan*
[9]*International Center for Materials Nanoarchitectonics, National Institute for Materials Science, 1-1 Namiki, Tsukuba 305-0044, Japan*

(Received 3 March 2022; accepted 14 June 2022; published 22 July 2022)

The excitonic states of transition metal dichalcogenide (TMD) monolayers are heavily influenced by their external dielectric environment and depend on the substrate used. In this work, various wide band gap dielectric materials, namely hexagonal boron nitride (*h*-BN) and amorphous silicon nitride (Si_3N_4), under different configurations as support or encapsulation material for WS_2 monolayers, are investigated to disentangle the factors contributing to inhomogeneous broadening of exciton absorption lines in TMDs using electron energy loss spectroscopy in a scanning transmission electron microscope. In addition, monolayer roughness in each configuration was determined from tilt series of electron diffraction patterns by assessing the broadening of diffraction spots by comparison with simulations. From our experiments, the main factors that play a role in linewidth broadening can be classified, in increasing order of importance, by monolayer roughness, surface cleanliness, and substrate-induced charge trapping. Furthermore, because high-energy electrons are used as a probe, electron-beam-induced damage on bare TMD monolayers is also revealed to be responsible for irreversible linewidth increases. *h*-BN not only provides clean surfaces of TMD monolayers and minimal charge disorder, but can also protect the TMD from irradiation damage. This work provides a better understanding of the mechanisms by which *h*-BN remains, to date, the most compatible material for 2D material encapsulation, facilitating the realization of intrinsic material properties to their full potential.

DOI: 10.1103/PhysRevMaterials.6.074005

I. INTRODUCTION

Two-dimensional materials have attracted the interest of a large portion of the solid state physics and nanoscience communities since the first production of atomically thin graphene layers [1]. This was in great part due to the novel physical properties which became accessible in these van der Waals materials as a function of thickness. Among the large class of such materials [2], transition metal dichalcogenide (TMD) monolayers specifically have been widely studied. Monolayers of these materials with the form MX_2 ($M =$ W or Mo and $X =$ S or Se) and the $2H$ phase are direct band gap semiconductors [3–6]. More interestingly, the exciton binding energy in them is large (hundreds of meV) [7,8], allowing excitons to survive up to high temperatures. The lowest-energy excitons are formed by bands close to the K and K' points. The d-orbital character from the transition metal of these bands leads to strong spin-orbit coupling, which forms two distinct excitons, denoted X_A and X_B here, with large energy separation (from 80 to 400 meV) [9]. Furthermore, the spin-valley states created by the combination of the crystal structure and spin-orbit interaction can be manipulated by polarized light beams [9–11].

Because of the decreased screening of the Coulomb interaction in 2D materials, their excitonic physics is different from that in 3D [12,13], with deviations from the Rydberg series for 3D materials [12,14,15]. Also due to the reduced screening, excitons in these materials are quite sensitive to the local dielectric environment [16,17] or strain [18], for example. Flat and clean samples are the key to preserve the intrinsic high optical quality of TMDs in practice [19,20]. This comes with the demand to control disorder as the optical response is heavily influenced by the external environment [21]. Moreover, suspended monolayers like graphene and MoS_2 have an intrinsic rippling nature [22–26]. A freestanding

---

[*] luiz.galvao-tizei@universite-paris-saclay.fr

monolayer has been observed to have an intrinsic corrugation, in other words, an atomic-scale roughness. For example, low energy electron diffraction (LEED) has demonstrated that suspended 2*H*-MoS_2 monolayer has surface corrugation that decreases with increasing number of layers [22]. It has been observed that encapsulation in *h*-BN significantly improves the properties of 2D materials, including better charge density homogeneity [27], higher carrier mobility [28], and sharper emission [19] and absorption linewidths [20]. The *h*-BN encapsulated TMD excitonic linewidth can approach the homogeneous broadening limit [19,29–31]. The influence of the *h*-BN encapsulation is attributed to the disorder minimization [21]. The exact reasons why *h*-BN encapsulation improves the electrical and optical properties of TMDs are not completely known. Atomic flatness of *h*-BN is observed to play a role in several transport experiments of graphene encapsulated in *h*-BN [32–34]. Furthermore, electron diffraction experiments have shown that *h*-BN encapsulated graphene [24–26] has a much smaller mean roughness (12 ± 5 pm) than a freestanding monolayer (114 ± 1 pm) [25]. The observed roughness of encapsulated graphene is comparable to the 27 pm found in scanning tunneling microscopy (STM) and grazing incidence fast atom diffraction measurements on epitaxial graphene on SiC [35,36]. Another clear benefit of encapsulation is the movement of surface residue and subsequent gathering into bubbles, which ensures that clean areas are available [37].

Optical techniques [optical absorption or photoluminescence (PL)] are typically used to study TMDs. Spectroscopic techniques using the electron beam could provide much higher spatial resolution to study optical behavior [38–40], which could provide greater understanding about the role of substrates and residue, when coupled to atomically resolved imaging techniques [20]. Electron energy loss spectroscopy (EELS) has not been widely used to probe the optical properties of TMD monolayers, with only a handful of reports in the literature [41–47]. A large part of the lack of interest in this technique was the observation of large absorption linewidths, above 150 meV at full width at half maximum (FWHM), which is considerably larger than one would expect even for room temperature optical measurements. Recently, EELS experiments of *h*-BN encapsulated WS_2 have shown that X_A linewidths can be much narrower (FWHM below 30 meV) [20], approaching values comparable to those measured using optical absorption at similar temperatures around 110 K [48]. A recent PL study of $MoSe_2$ observed linewidths of 45 meV in PL and 55 meV in STM under ambient conditions at room temperature [49].

In this work, we explore WS_2 monolayers on different substrate configurations (freestanding, *h*-BN, and Si_3N_4) with the objective to understand the possible effects leading to absorption linewidth broadening (in particular in EELS spectra). Our conclusions show that indeed monolayer roughness and surface residue are crucial to understand the line broadening in TMD monolayers. We also show that charge inhomogeneity due to charge trapping can lead to linewidth increase, depending on the substrate used. The series of monolayer configurations used allowed us to qualitatively pinpoint which effects are dominant for linewidth broadening. The increasing order of importance on linewidth is TMD roughness, surface residue, and substrate charge trapping. Lastly, the effects of electron-beam-induced damage to the absorption linewidth of the WS_2 monolayer on Si_3N_4 are also demonstrated.

The paper is organized into sections describing each of the underlying effects. A description of the experiment and the sample fabrication is given in Sec. II. The absorption linewidths for freestanding, 15-nm *h*-BN supported, 5-nm and 15-nm *h*-BN encapsulated, 15-nm Si_3N_4 supported, and 15-nm Si_3N_4/50-nm *h*-BN encapsulated WS_2 monolayers are reported in Sec. III. In Secs. IV, V, and VI, we discuss the role of monolayer roughness, substrate charging, and electron-beam-induced damage on absorption linewidth broadening. Then, a comparison and summary of the effects of the various factors on linewidth, and their ranking of importance, are presented in Sec. VII. Finally, the conclusions are presented in Sec. VIII.

II. METHODS

Experiments were performed in a scanning transmission electron microscope (STEM) called ChromaTEM, a modified Nion HERMES 200 equipped with an electron monochromator that allows for energy spreads down to below 10 meV at 60 keV and a side entry stage that can cool the sample down to 110 K. The electron beam energy is set at 60 keV for both EELS and diffraction measurements.

The convergence and collection half-angles for the EELS measurement are 10 mrad and 21 mrad, respectively. The EELS spectrometer dispersion was 4.46 meV/pixel, recorded onto a Princeton Instruments KURO CMOS detector with a 2048 × 2048 pixel array. Two types of spectra are measured in this paper: slow-scan and fast-scan EELS. In order to distinguish between the beam scan rate and the detector accumulation period, sampling dwell time and exposure time are used to sketch the two different scan modes, namely slow scan and fast scan. The sampling dwell time describes how long the beam stays at each scan position before moving to the next position, whereas exposure time is the detector accumulation time for each spectrum. Typical exposure time for slow scan is 150–500 ms per spectrum, with the CMOS detector exposure time the same as the sample dwell time, typical of a scanning/detector scheme for STEM-EELS spectrum imaging. For fast scan, the beam rasters on top of the sample at a speed of 1 μs/pixel, such that each spectrum is averaged across the full scanned area (a few hundred nm^2). All measurements for freestanding WS_2 monolayers are made in slow-scan mode, while for Si_3N_4 supported and Si_3N_4/*h*-BN encapsulated WS_2 monolayers, both types of measurements are performed (see further details in Sec. V). The convergence half-angle was set to 1 mrad to approximate an almost parallel beam in TEM for the diffraction measurements, and beam diameter is larger than 100 nm. The exposure time is 100 or 300 ms for the diffraction patterns. To reveal the effect of monolayer roughness, tilt series of electron diffraction patterns were acquired, with the sample tilted along the sample holder axis from 0 mrad to 385 mrad (≈22°) with 35 mrad (≈2°) step as demonstrated similarly for graphene [24,25].

The samples are made by the viscoelastic stamp method as reported for building van der Waals heterostructures [50,51]. *h*-BN was mechanically exfoliated with Scotch tape from bulk monocrystals. WS_2 was either exfoliated with Nitto blue tape

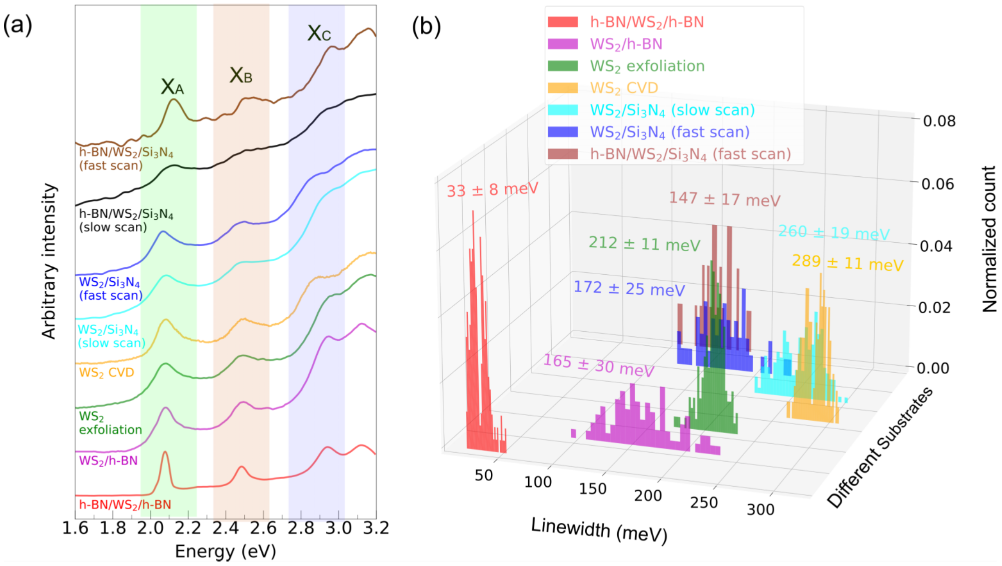

FIG. 1. EELS absorption spectrum and X_A FWHM histogram of monolayer WS_2 in various configurations. (a) EELS absorption spectra are measured by STEM-EELS on different substrates at 110 K. EELS spectra are from WS_2 monolayers of *h*-BN encapsulated (red), *h*-BN supported (purple), freestanding exfoliated (green), freestanding CVD-grown (yellow), slow-scan Si_3N_4 supported (cyan), fast-scan Si_3N_4 supported (blue), slow-scan Si_3N_4/h-BN encapsulated (black), and fast-scan Si_3N_4/h-BN encapsulated (brown) cases, respectively. Each spectrum is normalized with respect to its X_A intensity after zero-loss peak alignment and tail subtraction. (b) Histograms of X_A linewidths measured from different positions of WS_2 monolayer on different substrates. Linewidth is extracted from the FWHM of the Lorentzian fit of X_A exciton peak. The mean FWHM and standard deviation for each substrate are listed in the legend. Unfortunately, the excitons in slow-scan EELS spectrum of Si_3N_4/h-BN encapsulated WS_2 monolayer are too weak to fit with the strong background of *h*-BN, so there is no histogram for X_A in this configuration.

or grown by chemical vapor deposition (CVD). 15-nm-thick Si_3N_4 is provided by a commercial continuous support film TEM grid (PELCO). Aside from the Si_3N_4 series samples, the exfoliated WS_2 monolayer sample is transferred onto PELCO holey Si_3N_4 support film of 200 nm thickness, while all other samples were put on top of commercial Mo-supported Quantifoil holey carbon grids. More details are shown in Sec. S1 in the Supplemental Material [52].

III. EXCITONIC ABSORPTION LINEWIDTHS ON DIFFERENT SUBSTRATES

Exciton linewidth is influenced by several factors, such as the roughness of the monolayer, sample cleanliness, and dielectric environment homogeneity. *h*-BN has been shown to be an effective candidate in reducing the absorption and emission linewidths in TMD monolayers [19,29,30]. How does encapsulation with *h*-BN improve the optical quality of TMDs? Here, to answer this question, we explored WS_2 monolayers in different configurations: (i) freestanding, (ii) on *h*-BN, (iii) *h*-BN encapsulated, (iv) on Si_3N_4, and (v) Si_3N_4/h-BN encapsulated. In our experiment, three peaks (marked X_A, X_B, and X_C in Fig. 1) can be distinguished in all WS_2 monolayers on different substrates. A and B excitons are associated with transitions in the direct band gap between the K and K' points and are split due to spin-orbit coupling, denoted as X_A and X_B. C excitons are associated with direct transitions at the Q point between the Γ and K points in the Brillouin zone [53]. In this paper, we mainly focus on the linewidths of X_A and X_B, since they are easily distinguishable and do not overlap. Typical exciton linewidths in various ∼micrometer-wide suspended TMD monolayers are estimated above 150 meV at FWHM in EELS [41,43,44,46], at both 150 and 300 K, whereas encapsulated TMD monolayers show considerably sharper EELS absorption lines, 30 meV FWHM or below at 150 K [20], on par with optics [48,54].

The absorption EELS spectrum of the WS_2 monolayer changes for different substrate configurations at 110 K (Fig. 1). Small energy shifts occur due to different real parts of the dielectric function of the substrate and to strain. More evident is the large variation in width of the absorption peaks, in particular toward the lowest-energy transition of X_A. This can be quantified by the FWHM measured from spectral fits using Lorentzian functions. As shown in Fig. 1(b), the use of *h*-BN induces an obvious improvement in optical quality in comparison to both freestanding and Si_3N_4 supported monolayers, despite Si_3N_4 also being a wide-gap dielectric material. For the *h*-BN encapsulated WS_2 monolayer, the sharpest X_A mean absorption FWHM is observed. This is significantly less than the mean linewidth for the *h*-BN supported WS_2 monolayer which exhibits comparable TMD roughness (details for roughness are presented later in Sec. IV). It is known that in van der Waals heterostructures, interfaces between materials tend to expel residues, which then coalesce into bubbles [37]. Contamination could change the local dielectric function; thus the exciton peak center would shift and cause inhomogeneous broadening: a sum of different spectra with different energy centers. Therefore, a monolayer that is only supported on one side has an exposed surface and contains inhomogeneously distributed residue and adsorbates, which would explain the difference in X_A mean FWHM between the *h*-BN supported and encapsulated monolayers. Another

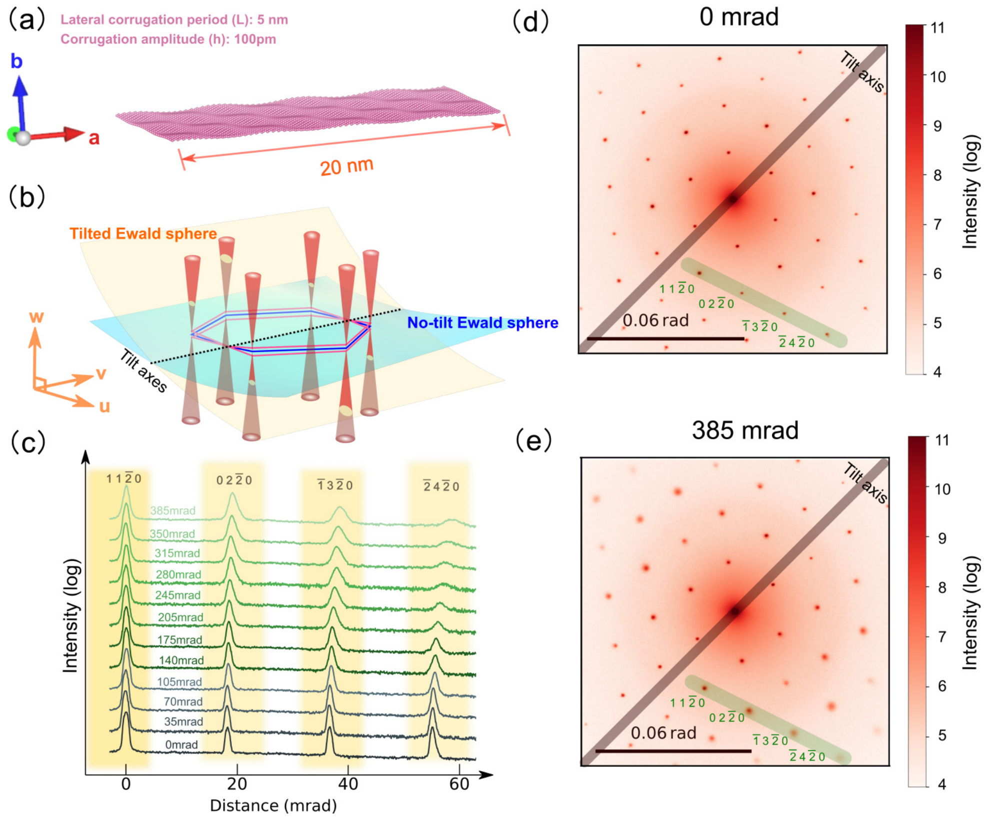

FIG. 2. (a) Model for a rippled WS_2 monolayer (only W atoms shown for visibility) displayed using VESTA [55]. (b) The reciprocal lattice of a rippled TMD monolayer is a set of cones (in red) due to the angular distribution of real-space lattice normal vectors. Also shown are two curved planes which approximate the surface of the Ewald sphere, indicating the points of intersection with the reciprocal space lattice to form the diffraction pattern. The blue plane shows the intersection at zero sample tilt, while the yellow plane shows the intersection at a nonzero tilt angle. The intersection geometry leads to two distinctly different diffraction patterns (d) for zero tilt and (e) for a tilted sample where the spots have become diffuse for a freestanding exfoliated WS_2 monolayer. (c) The intensity profiles of the four diffraction spots, which are indicated in (d) and (e) by the green bar, plotted in log scale. The tilt angle is from 0 mrad to 385 mrad with a step size of 35 mrad.

supporting evidence is that the *h*-BN and Si_3N_4 encapsulated WS_2 monolayer has sharper linewidth (147 meV) than *h*-BN supported WS_2 (165 meV), since the encapsulated monolayer has better surface cleanliness than the supported monolayer. In the next sections, we will explore in greater detail the effect of different substrates to gather more evidence concerning the benefits of *h*-BN encapsulation for TMD monolayers. In short, a combination of factors play a role, some more than others.

IV. MONOLAYER ROUGHNESS ON DIFFERENT SUBSTRATES

Suspended monolayers have an intrinsic nanoscale corrugation arising from their low-dimensional nature [22–26]. In addition, sample preparation and transfer protocols to substrates or TEM grids can also result in increased surface corrugation due to changes in temperature and surface tension from solvents used. We have observed that freestanding TMD monolayers produced by CVD or mechanical exfoliation have this nonflat fundamental property as illustrated in Fig. 2(a). Atomically thin monolayer corrugation can be detected using electron diffraction [24,25], as it can give access to information from the full 3D reciprocal space. In brief, a perfectly flat monolayer should have diffraction spot widths that do not change as the monolayer is tilted with respect to the electron beam. In contrast, a corrugated monolayer would show broadening of diffraction spots as a function of tilt angle as in Fig. 2(c).

To understand this, two points about electron diffraction in thin, corrugated materials should be understood. First of all, because the dimension of the object along the beam propagation direction is small, the reciprocal lattice points along this direction extend more significantly than in thick materials. As shown in Figs. 3(k) and 3(l), the green dots are the reciprocal lattice points of a thick material, whereas they are elongated into reciprocal lattice rods (or relrods [56]) in red in thin materials. Because they are extended in reciprocal space, the Bragg condition for diffraction is relaxed, meaning that electrons are diffracted even if they are not exactly at the diffraction condition. Thus the Ewald sphere intersects the reciprocal lattice points or relrods with excitation error $\boldsymbol{s} = \boldsymbol{K} - \boldsymbol{g}$ in this case, where $\boldsymbol{g}$ is the exact Bragg diffraction condition and $\boldsymbol{K}$ is the relaxed Bragg diffraction condition. For this reason, an atomically thin monolayer can be tilted substantially and still show large diffracted intensity and sharp peak width. Moreover, for a corrugated material, instead of relrods perpendicular to the real-space atomic plane, the reciprocal lattice consists of the superposition of relrods due to the real-space lattice normal vectors' tilt, leading to the formation of diffuse cones such as the red cones in Fig. 2(b) (in *u*-*v*-*w*

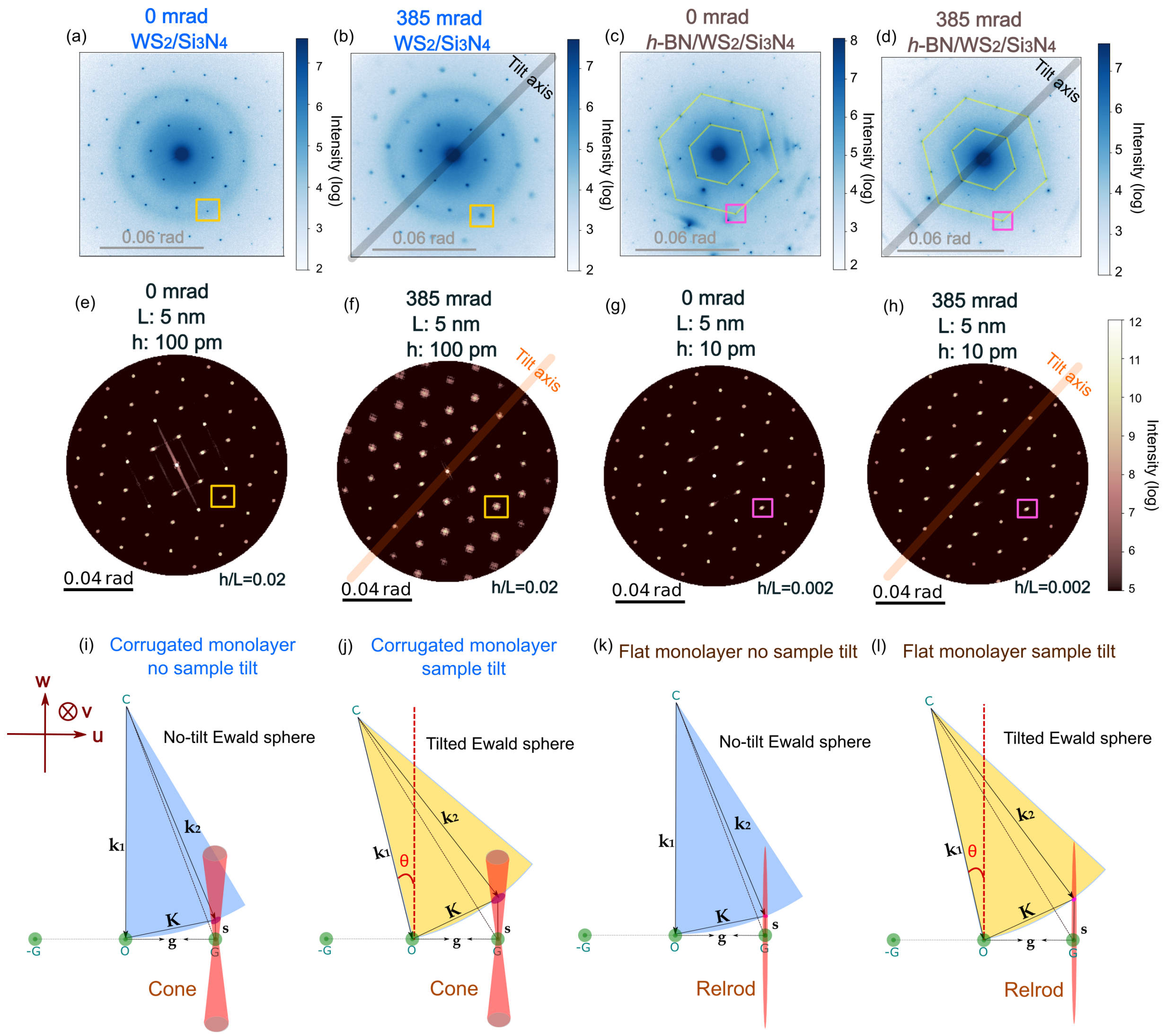

FIG. 3. (a) and (b) are experimental diffraction patterns at 0 mrad and 385 mrad for WS_2 monolayers supported by Si_3N_4. (c) and (d) are experimental diffraction patterns at 0 mrad and 385 mrad for WS_2 monolayer encapsulated by Si_3N_4/h-BN. (e) and (f) are the simulation results of $h/L = 0.02$ corrugation at 0 mrad and 385 mrad. Its peak size increased consistently with (a) and (b), as highlighted by the $\langle 02\bar{2}0\rangle$ spots boxed in yellow. (g) and (h) are the simulation results of $h/L = 0.002$ corrugation at 0 mrad and 385 mrad. Its peak size did not increase, consistent with (c) and (d), also highlighted by the $\langle 02\bar{2}0\rangle$ spots boxed in pink. The in-plane rotation and the tilt axis with respect to the first-order reflections in the simulations were chosen arbitrarily; only the tilt axis direction matches with the experiments in this case. (i) and (j) are the reciprocal space of a corrugated monolayer, corresponding to the diffraction patterns in (a), (e) and (b), (f). (k) and (l) are the reciprocal space of a flat monolayer, corresponding the diffraction pattern in (c), (g) and (d), (h). The Ewald sphere is plotted with radius k (the difference between incident electron momentum $\mathbf{k_1}$ and deflected electron momentum $\mathbf{k_2}$ is very small, so $k = |\mathbf{k_1}| \approx |\mathbf{k_2}|$) in yellow (tilted sample) and blue (no sample tilt); θ in red is the sample tilt angle in (j) and (l). Bragg diffraction condition is relaxed in all atomically thin materials, whether it is flat or corrugated. $\mathbf{K} = \mathbf{g} + \mathbf{s} = \mathbf{k_2} - \mathbf{k_1}$, where the value of $\mathbf{g}$ is the inverse of the $\langle 02\bar{2}0\rangle$ interplanar distance and $\mathbf{s}$ is the vector to describe how far $\mathbf{K}$ deviates from the exact Bragg condition.

space) and Figs. 3(i) and 3(j) (in the u-w plane). The schematic in Fig. 2(b) and Figs. 3(i) and 3(j) illustrates how the Ewald sphere intersects with the reciprocal lattice cones of a rippled monolayer when electrons are incident perpendicularly (zero sample tilt) and nonperpendicularly on the sample (tilted sample). If the sample is not tilted, the Ewald sphere [blue plane in Fig. 2(b)] intersects the vertices of the conjoined cones, marked by the blue hexagon in Fig. 2(b). If the sample is tilted, the Ewald sphere [yellow plane in Fig. 2(b)] intersects the cones at a certain height along the w axis, denoted by the yellow ovals on the cones. In Figs. 3(i) and 3(l), only one relrod/cone is drawn to show the relaxed Bragg diffraction for flat and corrugated thin material at no sample tilt and tilted sample diffraction configurations.

Now that we have explained how roughness measurements were performed, we turn to the measurements for different substrates, to try to relate possible variations to the observed linewidth differences seen in the EELS spectra. To compare the roughness of TMD monolayers when placed on or encapsulated in different substrates, we measured the diffraction

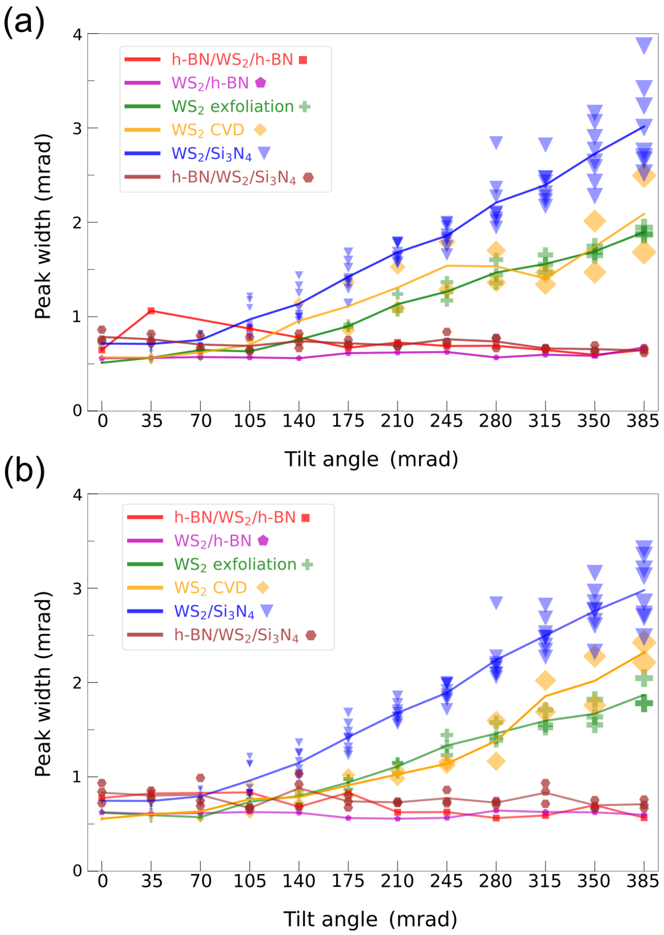

FIG. 4. Roughness measurement of WS_2 monolayers for various substrate configurations of *h*-BN encapsulated (red), *h*-BN supported (purple), freestanding exfoliated (green), freestanding CVD-grown (yellow), Si_3N_4 supported (blue), and Si_3N_4/*h*-BN encapsulated (brown) cases. The peak width is extracted from a 2D Gaussian fit of specific diffraction spots in each diffraction pattern, represented by different geometries and colors. The lines indicate the average value of the peak width on different substrates at each angle in the cases of multiple measurements from different regions. (a) FWHM of peak width change with tilt angle along *x* direction. (b) FWHM of peak width change with tilt angle along *y* direction. See the candidate peaks and fit details in Sec. S4 in the Supplemental Material [52].

spot width evolution in a tilt series with steps of 35 mrad (or ≈2°) from 0 mrad up to 385 mrad (or ≈22°), as shown in Fig. 4. The width of diffraction spots was retrieved from the FWHM of a 2D Gaussian fit presented in Sec. S4 in the Supplemental Material [52]. The 2D Gaussian fit was made at linear intensity scale as they are true values, whereas the plot in Fig. 2 is shown in log intensity scale to suppress the central spot and enhance weak higher-order spots so that they can be visualized on the same plot.

For the freestanding monolayer and Si_3N_4 supported monolayer, the width of the diffraction spots quickly increased, with a maximum width when the monolayer is tilted to the maximum angle of 385 mrad, as shown in Fig. 4 (green, yellow, and blue lines). The diffraction spot width barely changes as a function of tilt when the monolayer is encapsulated or supported by *h*-BN as in Fig. 4 (red, purple, and brown lines) and Figs. 3(c) and 3(d). Both a single thin layer of 15-nm *h*-BN (supported monolayer) or full *h*-BN encapsulation reduces roughness, producing a flat WS_2 monolayer, as shown in Fig. S6 [52]. The roughness of a WS_2 monolayer in different configurations from the roughest to flattest is as follows: Si_3N_4 supported, freestanding, *h*-BN on one or both sides.

To confirm that the diffraction spot broadening can be explained by the TMD monolayer roughness, we have performed numerical calculations for the expected diffraction patterns of rough and flat monolayers using QSTEM (quantitative TEM/STEM simulations software) [57]. In the atomic model, the roughness was simulated by a product of two trigonometric functions, but the real pattern is most probably more complex. This might explain why the symmetry of the spots observed in experiments does not always match the symmetry observed in simulations. Despite not being relaxed, these model structures are sufficient to view the effect of roughness on the diffraction patterns and estimate the amplitude of the monolayer rippling. The results of the simulations indicate that the typical height (h) for the corrugation roughness equals 0.01 times the lateral corrugation period (L), or $0.01 \times L$, for the freestanding monolayer, $0.02 \times L$ for the monolayer on Si_3N_4, and less than $0.002 \times L$ for the monolayer supported by and encapsulated in *h*-BN, as shown in Fig. S4 and Fig. S5 [52]. Our simulation thus only provides an estimate for the average roughness amplitude; more details are described in the Supplemental Material [52].

These measurements indicate that *h*-BN as a substrate suppresses the intrinsic roughness of the TMD monolayer and thus ensures the flatness of a TMD monolayer, showing at least 20× reduction in roughness even when used in conjunction on top of rough substrates such as Si_3N_4 (diffraction patterns shown in Fig. S6 [52]). This is expected, in view of previous experiments with *h*-BN encapsulation of graphene and optical experiments of encapsulated TMDs [48,54,58–60]. A WS_2 monolayer on top of the Si_3N_4 is expected to be rough, as this amorphous substrate is not flat, with mean roughness of ~400 pm measured by atomic-force microscopy. This is confirmed using electron diffraction, as summarized in Figs. 3(a) and 3(b) and Fig. 4. A separate region of the same WS_2 CVD monolayer on Si_3N_4 covered by a thin *h*-BN layer shows a diffraction pattern with similar spot widths to the *h*-BN encapsulated monolayer, at all sample tilts as shown in Figs. 3(c) and 3(d) and Fig. 4. This allows the construction of high-quality devices on top of different substrates, even if the substrate itself is rough (at least with roughness comparable to that of the amorphous Si_3N_4), to obtain a flat TMD monolayer by the use of single top layer *h*-BN.

V. EFFECT OF DOSE RATE ON CHARGING

The monolayer supported by Si_3N_4 is not flat, as discussed in the previous section, which explains the large FWHM for the X_A reported in Fig. 1. If monolayer roughness was the only cause for the linewidth broadening, one would expect to measure sharper X_A absorption lines on the sample which is covered by a thin *h*-BN layer with low monolayer roughness (Fig. 4 data points in brown). A reduction is

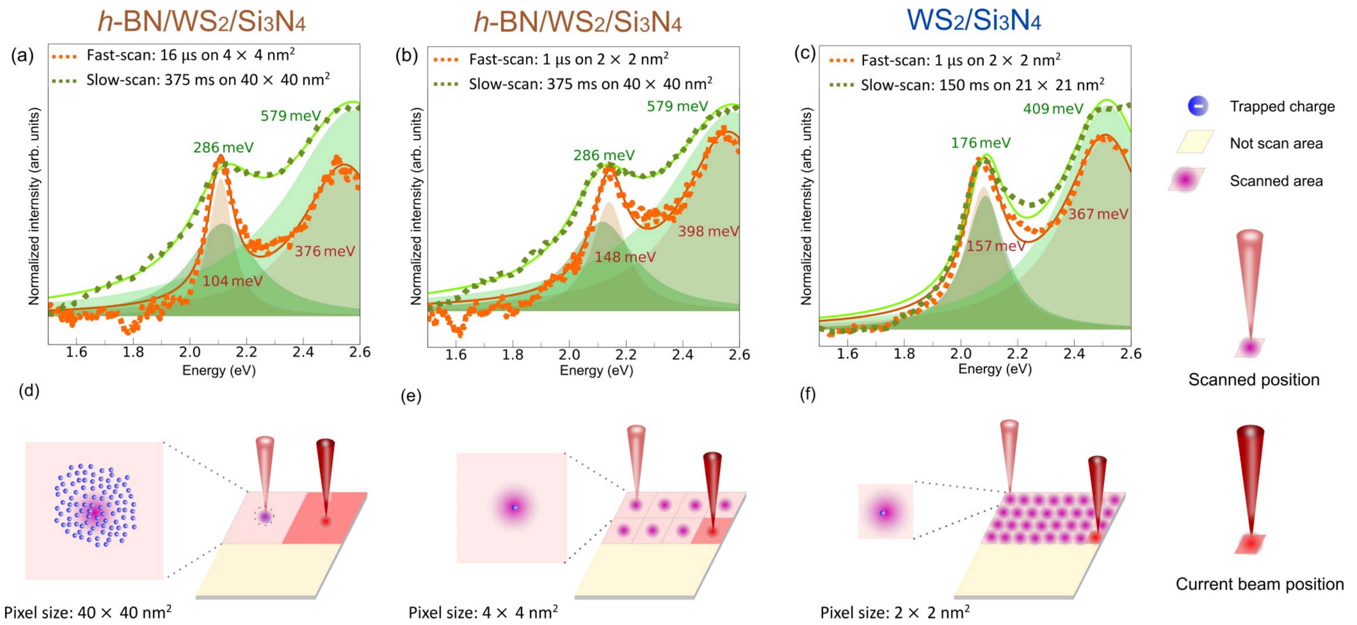

FIG. 5. (a) Slow scan vs fast scan in h-BN/WS$_2$/Si$_3$N$_4$: Spectra comparison between slow-scan (green dotted line) and fast-scan (orange dotted line) acquisition. The pixel dwell times are 375 ms and 16 μs and the pixel sizes are 40×40 nm^2 and 4×4 nm^2, respectively. The linewidth is given by the FWHM of a Lorenzian fit of X_A and X_B peaks as labeled; solid line is the sum of the fitted curves of the two excitations and the offset. (b) Slow scan vs fast scan (1 μs on 2×2 nm^2) in h-BN/WS$_2$/Si$_3$N$_4$: The linewidth of X_A and X_B in fast scan (1 μs on 2×2 nm^2) is 148 meV and 398 meV. Linewidth of X_A is wider than fast scan (16 μs on 4×4 nm^2), but sharper than slow scan (375 ms on 40×40 nm^2 area). (c) Slow scan vs fast scan (1 μs on 2×2 nm^2) in WS$_2$/Si$_3$N$_4$: The linewidths of X_A and X_B are as labeled. (d) The scan patterns correspond to slow-scan mode: 100 ms dwell time on a 40 nm^2 sized pixel, the most residual charges induced by fast beam. (e) The scan patterns correspond to large pixel scan patterns: μs dwell time on 4×4 nm^2 pixel, the least residual charges induced by fast beam. The linewidth is the closest to intrinsic linewidth. (f) The scan patterns correspond to small pixel scan patterns: 1 μs dwell time on 2×2 nm^2 pixel, less residual charges than slow scan but more residual charges than large pixel fast scan.

observed in Fig. 1(b) from 172 meV to 147 meV in FWHM (mean values of the histogram) when comparing the same fast-scan rates, which is still significantly larger than observed in the h-BN encapsulated sample (33 meV on average).

During the EELS experiments, it was observed that the measured FWHM of the X_A absorption peak for WS$_2$ across Si$_3$N$_4$ depended on how the electron beam was scanned on the samples. We note that the 15-nm-thick Si$_3$N$_4$ layer used to support the WS$_2$ monolayer is an insulator, which is known to be prone to charge accumulation. This would lead to a local shift of the exciton line and inhomogeneous broadening, explaining our observations. The important parameters here are the scan speed (how long the beam dwells at a specific pixel before moving to next pixel), spatial sampling (the distance between neighboring pixels), and total scanned area size. To test and control this effect, we acquired spectra with the same total acquisition times and total scanned area size, while the electron beam was scanned at different rates and sampling on the TMD monolayer.

Using acquisition settings typical of EELS spectrum imaging (slow scan), a dwell time on a 100 ms timescale, with an approximately 1-nm-wide beam and a sampling on the order of 10 nm/pixel, the X_A was systematically broader than the fast scan as presented in Figs. 5(a)–5(c) (green curves). In comparison to spectra acquired over identical regions where the electron beam was rastered at much faster speeds (sample dwell time of 1–16 μs/pixel) while keeping the exposure time constant, the linewidths can be decreased by more than half [orange curves in Figs. 5(a)–5(c)]. The spectral evolution due to these changes in scan parameters is summarized schematically in Figs. 5(d)–5(f). Globally, typical EELS spectrum imaging acquisition leads to long dwell times for the electron beam, which allows the charges to be trapped (according to our interpretation) in the Si$_3$N$_4$ substrate, represented by little purple dots in Fig. 5(d). The pink and red cones represent the electron beam raster start and finish positions, respectively, while the shaded pink and red areas in the specimen plane represent areas scanned by the electron beam and current scan areas. One immediately sees in Figs. 5(e) and 5(f) that increasing the scan speed and the sampling can distribute these trapped charges more homogeneously across a larger area, reducing their overall effect. 15-nm Si$_3$N$_4$-windowed TEM grids are routinely used for EELS experiments of plasmonic materials, with their charging under the electron irradiation a known limitation, which leads to electron beam displacement with respect to the sample (seen as spatial drift during data acquisition). h-BN, while also an insulator on the other hand, has been shown to be a valid alternative, which does not possess this limitation [61].

To obtain the intrinsic exciton linewidth in this sample, we utilized scanning parameters denoted as the fast-scan mode, in which the sampling is 4 nm/pixel and the scan speed 16 μs/pixel. At the same time, with the beam scanning, EELS spectra were acquired using the same detector accumulation time of 100 ms/spectrum as in the slow-scan mode. The X_A linewidth with the slow-scan scheme is 286 meV. The faster scan rate produces a sharper X_A linewidth (104 meV). This is reproduced in different areas of the same sample, albeit with small changes in spatial sampling, showing similar behavior in Figs. 5(a) and 5(b).

To check whether the X_A absorption broadening was due to the roughness of the WS_2 monolayer on Si_3N_4, a part of this sample was covered with 50-nm-thick *h*-BN. Indeed, roughness is reduced by the presence of *h*-BN, as described in the previous section. In these regions, the initial X_A FWHM for slow-scan acquisitions is narrower than in the regions only supported on Si_3N_4, but the overall reduction from fast scanning is not more pronounced than in the Si_3N_4 sample. This indicates that other effects are playing a role. Electron diffraction rules out a difference in roughness, but residual effects due to charge trapping accumulated between measurements over the same area without discharging, despite modifying the scanning parameters, could still increase the linewidth. As we will explain further in the next section, electron-beam-induced damage in the Si_3N_4 supported sample also leads to linewidth broadening.

In this section, we discussed the effect of different scan rates on the X_A linewidth of a WS_2 monolayer supported by Si_3N_4. Interestingly, the same charging effect is not observed on *h*-BN supported or encapsulated monolayers, despite the fact that both materials are insulators and *h*-BN has a larger band gap than Si_3N_4. Other factors such as the low intrinsic disorder of crystalline *h*-BN, i.e., low density of atomic defects, makes it a better candidate to counteract against surface charge effects on TMDs. Amorphous Si_3N_4 on the other hand can exhibit extrinsic charge disorder similarly to SiO_2, depending on its defect density and impurities, including hosting trapped charges and surface adsorbates [62,63]. We note that these experiments were performed with electron current between 1–20 pA in a monochromated electron microscope. Experiments were attempted to reversibly control the observed charge trapping. However, the magnitude of the broadening produced at fixed currents varied at different sample positions. We could not identify underlying reasons for these changes. For this reason, a quantitative assessment of the charge trapping was not possible.

VI. EFFECT OF ELECTRON BEAM DAMAGE

A final broadening mechanism that we identified is irradiation damage, i.e., electron-beam-induced damage in the case of EELS. 60 keV and higher kinetic energy electrons are known to induce damage on TMD samples through either elastic or inelastic scattering. The first mechanism, known as knock-on [64–66], leads to the removal of atoms. It is more effective at higher kinetic energies [64] and should present a cutoff at lower energies, below which knock-on should not be possible, as not enough energy would be available to eject the atom. However, due to the thermal motion of atoms [65,66], knock-on damage can still occur below this threshold. Electronic excitations can also induce below threshold atom removal [67]. The cutoff is proportional to the atomic mass, as the maximum energy transferred during elastic scattering decreases as the ratio between the mass of the electron and the target atom increases [64]. For this reason, knock-on of heavy atoms (compared to carbon, whose cutoff is 86 keV [68]) should be an ineffective damage mechanism, as in WS_2. However, the preexistence of defects can decrease the energy necessary for knock-on, allowing atom removal from edges or voids [69].

Inelastic scattering leads to the material modification through high-energy transfer, which can lead to bond breaking and atomic motion. The cross section for these events increases at lower kinetic energies for the incident electron beam [64] and is thus an effective mechanism for beam damage in TMDs. Typically for TMDs, it has been found that a good compromise for electron microscopy and spectroscopy experiments is to use electron beams with kinetic energy between 60 and 100 keV [20,41]. Here we chose to use 60 keV, which also minimizes damage on the *h*-BN encapsulation layer.

In the experiments here and others reported by some of the current authors [20], in addition to the sharp linewidth of the X_A, it was also seen that beam damage is significantly reduced in *h*-BN encapsulated TMD monolayers, allowing even the imaging and spectroscopy of stable monolayer edges. Nonetheless, this is not true for all substrates. In the Si_3N_4 supported monolayers, beam damage does occur. This appears as a linewidth broadening as a function of repeated irradiation, which is not reversible by subsequently leaving the measured area unexposed to the electron beam for certain periods. This is in contrast to the mechanism described in the previous section, where trapped charges are recombined, leading to reduction of the X_A linewidth if the electron beam is moved away and then faster scan acquisitions are performed.

EELS spectra for the same region of WS_2 supported on Si_3N_4 acquired in series show an increase in the X_A linewidth [Fig. 6(a)]. These spectra are averaged from two 70 × 44 pixel EELS data cubes with pixel size of 21×21 nm^2 and exposure time 150 ms. The effect of the first scan was to induce damage and increase the linewidth from 167 meV to 200 meV. One could argue that this was due to charge trapped in the Si_3N_4. Unfortunately, this broadening is not recovered by subsequently leaving the area unexposed to the electron beam. Another test for this hypothesis is the sequential acquisition of spectra in a fast-scan mode (as described in the previous section), with different scan rates. If the induced broadening is reversible, this would indicate that it was due to charging and not permanent crystal damage. This does not occur for the WS_2 monolayer on Si_3N_4. A sequence of acquisitions with fixed scan area and pixel size (2×2 nm^2) with sample dwell time 1, 4, 16, 64, and 1 μs shows an increasingly broader X_A absorption peak [from 151 to 184 meV; Fig. 6(b)], which is not reduced during the last fast-scan acquisition. The irreversible X_A linewidth increase is not observed for the sample encapsulated in Si_3N_4/h-BN [Fig. 6(c)].

VII. DISCUSSION OF DOMINANT EFFECTS ON LINEWIDTH

In the previous sections we described how various effects influence the EELS linewidth of WS_2 excitons in different configurations. In fact, any parameter modifying the energy position of the absorption peak will lead to linewidth broadening. For example, one can cite in this regard dielectric

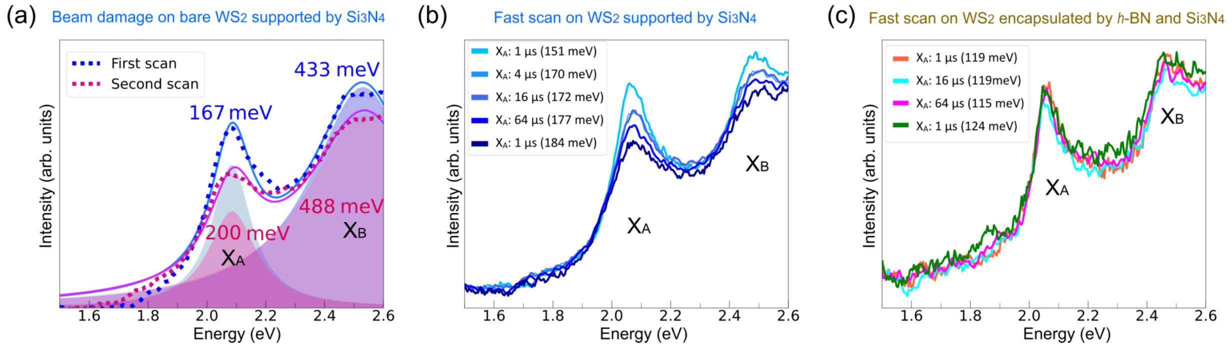

FIG. 6. (a) WS_2 on Si_3N_4: Beam damage induces the broadening of WS_2 excitons under EELS slow scan with pixel size 21×21 nm^2 at 150 ms exposure time. (b) WS_2 on Si_3N_4: 2×2 μm^2 area fast scan with pixel size 2×2 nm^2; the area is scanned under the sample dwell time of 1, 4, 16, 64 μs and then back to 1 μs. Exciton peak broadening is because of charging and beam damage. (c) The WS_2 encapsulated between *h*-BN and Si_3N_4: 2×2 μm^2 area fast scan with pixel size 2×2 nm^2; the area is scanned under the sample dwell time of 1, 16, 64 μs and then back to 1 μs. There is no significant exciton peak broadening after several scans.

disorder, strain, and proximity to extended defects (voids or edges) present in the monolayer. By comparing the dominant effect from each substrate and the resulting linewidths (Table I) we can reach a qualitative classification of the importance of TMD roughness, TMD surface cleanliness, and substrate charge trapping on linewidth broadening. The comparable roughness (corrugation amplitude, *h*, as a function of corrugation period, *L*) for *h*-BN encapsulated, *h*-BN supported, and *h*-BN/Si_3N_4 encapsulated WS_2 shows that the monolayer flatness is not the prevailing factor among those considered here on linewidth. For instance, the flatter *h*-BN supported WS_2 shows a linewidth (165 meV) comparable to that of the rougher Si_3N_4 supported WS_2 configurations (172 meV).

In fact, both surface cleanliness and charge disorder have substantial influence on the linewidth of TMD excitons. Only when the TMD is fully protected against surface charge disorder, the presence of adsorbates, and randomly distributed residue (due to clean interfaces) between two *h*-BN flakes can the narrowest linewidth of 33 meV be obtained. Also, there is no variation in the linewidth of the excitons for either fast scan or slow scan in *h*-BN encapsulation, which further supports that *h*-BN is defect-free and therefore insensitive to residual charge from the electron beam. The linewidth broadening in the case of *h*-BN supported WS_2 (165 meV) can be attributed mostly to the lack of cleanliness of its remaining exposed surface.

For monolayer with a comparable surface residue (WS_2 on Si_3N_4), charge trapping on the substrate can significantly increase the linewidth, leading to its linewidth being sensitive to electron beam scanning modes. The effect of the trapped charge on the linewidth is most obvious in the slow-scan mode because it is difficult to discharge at large electron doses. This leads to the local conductivity and dielectric variations and thus inhomogeneous linewidth broadening. This charging effect is less pronounced under fast scan, where linewidth is reduced from 260 meV (slow scan) to 172 meV (fast scan). In the case where the charge effect is not obvious such as fast scan in WS_2 on Si_3N_4, its linewidth is similar to the linewidth of WS_2 on *h*-BN, since they both have one clean surface and the other exposed. With an addition of a top-layer *h*-BN, the linewidth is reduced to 147 meV, because both surfaces of WS_2 are now cleaner. Despite this, the linewidth is still not as narrow as *h*-BN encapsulated WS_2, because residual charges are inevitable from the amorphous Si_3N_4 even in the case of fast scan.

The linewidth of WS_2 on Si_3N_4 (260 meV) under slow-scan mode is larger than freestanding exfoliated WS_2 (212 meV). This comparison should be taken cautiously, as too much surface residue coupled with high roughness (freestanding CVD-grown WS_2) can lead to broader absorption lines (289 meV), although WS_2 monolayer corrugates more dramatically on Si_3N_4 than freestanding.

With these comparisons we conclude that the order of importance of these effect is as follows: monolayer roughness, followed by monolayer cleanliness and substrate charge inhomogeneity. It should be noted that the latter two can be

TABLE I. Summary of (WS_2 monolayer) X_A linewidths in different configurations.

Configuration	Surface cleanliness	Trapped charges	Roughness	Linewidth
h-BN/WS_2/*h*-BN	Both sides clean	Few	$0.002 \times L$	33 ± 8 meV
Si_3N_4/WS_2/*h*-BN	Both sides clean	Many	$0.002 \times L$	147 ± 17 meV (fast scan)
WS_2/*h*-BN	One side clean, one side dirty	Few	$0.002 \times L$	165 ± 30 meV
WS_2/Si_3N_4	One side clean, one side dirty	Many	$0.02 \times L$	172 ± 25 meV (fast scan), 260 ± 11 meV (slow scan)
Exfoliated WS_2 (freestanding)	Both sides dirty	Some	$0.01 \times L$	212 ± 11 meV
CVD-grown WS_2 (freestanding)	Both sides dirty	Some	$0.01 \times L$	289 ± 11 meV

correlated, and not so straightforwardly ranked in relation to the other in all situations.

VIII. CONCLUSION

We have explored the role of different substrates on the EELS absorption linewidths of WS_2 monolayers. We have identified four main possible broadening factors: (i) monolayer roughness, (ii) surface cleanliness, (iii) charge trapping in substrates, and (iv) electron-beam-induced damage.

The first three have been considered and discussed in the past for optical spectroscopies extensively [19,58,70]. The experiments described here give indications that these three effects on TMD absorption linewidth broadening are also applicable in electron spectroscopy, and can be ranked by decreasing order of dominance of substrate charge disorder, followed by surface cleanliness, then monolayer roughness. These findings conclude that *h*-BN remains, so far, the most suitable substrate for both optical and electron spectroscopies with TMD monolayers and atomically thin layers for multiple reasons. Clearly, surface cleanliness is crucial: encapsulation with *h*-BN on both surfaces is required to confine the surface residue into localized patches, as widely known in the 2D materials community. Moreover, monolayer flatness is influential to reducing X_A linewidth, as shown by our comparison of *h*-BN supported, *h*-BN encapsulated, and Si_3N_4/h-BN encapsulated WS_2 monolayers. However, flatness and cleanliness are clearly not enough as the WS_2 monolayer encapsulated in Si_3N_4/h-BN is flat and sufficiently clean but still has a significantly broader X_A absorption linewidth than the *h*-BN encapsulated WS_2 monolayer. Charge trapping on substrates also plays a key role, as exemplified by the experiments on Si_3N_4. We emphasize that these effects are not intrinsic to electron spectroscopy, and broadly applicable in a similar manner for optical spectroscopies. Trapping of charges in *h*-BN seems to be ineffective, indicating why it is such a good substrate for electron spectroscopy. Finally, electron-beam-induced damage also plays a considerable role for electron spectroscopy of 2D materials, intrinsically hindered by the use of an electron beam, but this detriment could be ignored when *h*-BN is on top of the TMD monolayer. The combination of these four characteristics explains the large linewidths observed in EELS experiments in the past [41–47].

The experiments reported here indicate a viable path for electron spectroscopy experiments with comparable energy resolution to optical measurements in the available temperature and energy ranges. At the time of writing, electron microscopes capable of 1 meV spectral resolution at liquid helium temperatures and with high spatial resolution are still not available. So a direct comparison with the best optical experiments is not yet possible.

ACKNOWLEDGMENTS

This project has been funded in part by the National Agency for Research under the program of future investment TEMPOS-CHROMATEM (Reference No. ANR-10-EQPX-50), MAGMA Research Grant No. ANR-16-CE09-0027, and the JCJC grant SpinE (Reference No. ANR-20-CE42-0020), by the National Key Technologies R&D Program of China (Grant No. 2018YFA0306100), and by the European Union's Horizon 2020 research and innovation program under Grant Agreements No. 823717 (ESTEEM3) and No. 101017720 (EBEAM). This work has been supported by Region Île-de-France in the framework of DIM SIRTEQ. F.S. acknowledges support by the China Scholarship Council. A.A. and B.J.C. acknowledge support by the Alexander von Humboldt Foundation. A.A. acknowledges funding from DFG Grant No. AR 1128/1 and NM-ICPS of the DST, Government of India through the I-HUB Quantum Technology Foundation (Pune, India). C.M. would like to acknowledge support through Royal Society University Research Fellowship No. UF160539 and the Research Fellow Enhancement Award No. 2017 (RGF/EA/180090) by the Royal Society UK. K.W. and T.T. acknowledge support from the Elemental Strategy Initiative conducted by MEXT, Japan (Grant No. JPMXP0112101001) and JSPS KAKENHI (Grants No. 19H05790, No. 20H00354, and No. 21H05233). The authors acknowledge S. Rohart for AFM measurements on Si_3N_4 thin films.

---

[1] A. K. Geim and K. S. Novoselov, The rise of graphene, in *Nanoscience and Technology: A Collection of Reviews from Nature Journals* (World Scientific, 2010), pp. 11–19.

[2] N. Mounet, M. Gibertini, P. Schwaller, D. Campi, A. Merkys, A. Marrazzo, T. Sohier, I. E. Castelli, A. Cepellotti, G. Pizzi *et al.*, Two-dimensional materials from high-throughput computational exfoliation of experimentally known compounds, Nat. Nanotechnol. **13**, 246 (2018).

[3] K. F. Mak, C. Lee, J. Hone, J. Shan, and T. F. Heinz, Atomically Thin MoS_2: A New Direct-Gap Semiconductor, Phys. Rev. Lett. **105**, 136805 (2010).

[4] A. Splendiani, L. Sun, Y. Zhang, T. Li, J. Kim, C.-Y. Chim, G. Galli, and F. Wang, Emerging photoluminescence in monolayer MoS_2, Nano Lett. **10**, 1271 (2010).

[5] T. Mueller and E. Malic, Exciton physics and device application of two-dimensional transition metal dichalcogenide semiconductors, npj 2D Mater. Appl. **2**, 29 (2018).

[6] G. Wang, A. Chernikov, M. M. Glazov, T. F. Heinz, X. Marie, T. Amand, and B. Urbaszek, Colloquium: Excitons in atomically thin transition metal dichalcogenides, Rev. Mod. Phys. **90**, 021001 (2018).

[7] M. M. Ugeda, A. J. Bradley, S.-F. Shi, H. Felipe, Y. Zhang, D. Y. Qiu, W. Ruan, S.-K. Mo, Z. Hussain, Z.-X. Shen, F. Wang, S. G. Louie, and M. F. Crommie, Giant bandgap renormalization and excitonic effects in a monolayer transition metal dichalcogenide semiconductor, Nat. Mater. **13**, 1091 (2014).

[8] A. Arora, Magneto-optics of layered two-dimensional semiconductors and heterostructures: Progress and prospects, J. Appl. Phys. **129**, 120902 (2021).

[9] D. Xiao, G.-B. Liu, W. Feng, X. Xu, and W. Yao, Coupled Spin and Valley Physics in Monolayers of MoS_2 and Other Group-VI Dichalcogenides, Phys. Rev. Lett. **108**, 196802 (2012).

[10] H. Zeng, J. Dai, W. Yao, D. Xiao, and X. Cui, Valley polarization in MoS_2 monolayers by optical pumping, Nat. Nanotechnol. **7**, 490 (2012).

[11] G. Sallen, L. Bouet, X. Marie, G. Wang, C. R. Zhu, W. P. Han, Y. Lu, P. H. Tan, T. Amand, B. L. Liu, and B. Urbaszek, Robust optical emission polarization in MoS_2 monolayers through selective valley excitation, Phys. Rev. B **86**, 081301(R) (2012).

[12] K. S. Thygesen, Calculating excitons, plasmons, and quasiparticles in 2D materials and van der Waals heterostructures, 2D Mater. **4**, 022004 (2017).

[13] P. Cudazzo, I. V. Tokatly, and A. Rubio, Dielectric screening in two-dimensional insulators: Implications for excitonic and impurity states in graphane, Phys. Rev. B **84**, 085406 (2011).

[14] A. Chernikov, T. C. Berkelbach, H. M. Hill, A. Rigosi, Y. Li, O. B. Aslan, D. R. Reichman, M. S. Hybertsen, and T. F. Heinz, Exciton Binding Energy and Nonhydrogenic Rydberg series in Monolayer WS_2, Phys. Rev. Lett. **113**, 076802 (2014).

[15] K. He, N. Kumar, L. Zhao, Z. Wang, K. F. Mak, H. Zhao, and J. Shan, Tightly Bound Excitons in Monolayer WSe_2, Phys. Rev. Lett. **113**, 026803 (2014).

[16] H. H. Fang, B. Han, C. Robert, M. A. Semina, D. Lagarde, E. Courtade, T. Taniguchi, K. Watanabe, T. Amand, B. Urbaszek, M. M. Glazov, and X. Marie, Control of the Exciton Radiative Lifetime in van der Waals Heterostructures, Phys. Rev. Lett. **123**, 067401 (2019).

[17] E. Lorchat, L. E. P. López, C. Robert, D. Lagarde, G. Froehlicher, T. Taniguchi, K. Watanabe, X. Marie, and S. Berciaud, Filtering the photoluminescence spectra of atomically thin semiconductors with graphene, Nat. Nanotechnol. **15**, 283 (2020).

[18] D. Andrzejewski, R. Oliver, Y. Beckmann, A. Grundmann, M. Heuken, H. Kalisch, A. Vescan, T. Kümmell, and G. Bacher, Flexible large-area light-emitting devices based on WS_2 monolayers, Adv. Opt. Mater. **8**, 2000694 (2020).

[19] F. Cadiz, E. Courtade, C. Robert, G. Wang, Y. Shen, H. Cai, T. Taniguchi, K. Watanabe, H. Carrere, D. Lagarde, M. Manca, T. Amand, P. Renucci, S. Tongay, X. Marie, and B. Urbaszek, Excitonic Linewidth Approaching the Homogeneous Limit in MoS_2-Based van der Waals Heterostructures, Phys. Rev. X **7**, 021026 (2017).

[20] N. Bonnet, H. Y. Lee, F. Shao, S. Y. Woo, J.-D. Blazit, K. Watanabe, T. Taniguchi, A. Zobelli, O. Stéphan, M. Kociak, S. Gradečak, and L. H. G. Tizei, Nanoscale modification of WS_2 trion emission by its local electromagnetic environment, Nano Lett. **21**, 10178 (2021).

[21] D. Rhodes, S. H. Chae, R. Ribeiro-Palau, and J. Hone, Disorder in van der Waals heterostructures of 2D materials, Nat. Mater. **18**, 541 (2019).

[22] Z. Dai, W. Jin, M. Grady, J. T. Sadowski, J. I. Dadap, R. M. Osgood Jr., and K. Pohl, Surface structure of bulk 2H-MoS_2(0001) and exfoliated suspended monolayer MoS_2: A selected area low energy electron diffraction study, Surf. Sci. **660**, 16 (2017).

[23] A. Locatelli, K. R. Knox, D. Cvetko, T. O. Mentes, M. A. Nino, S. Wang, M. B. Yilmaz, P. Kim, R. M. Osgood Jr., and A. Morgante, Corrugation in exfoliated graphene: An electron microscopy and diffraction study, ACS Nano **4**, 4879 (2010).

[24] J. C. Meyer, A. K. Geim, M. I. Katsnelson, K. S. Novoselov, T. J. Booth, and S. Roth, The structure of suspended graphene sheets, Nature (London) **446**, 60 (2007).

[25] J. D. Thomsen, T. Gunst, S. S. Gregersen, L. Gammelgaard, B. S. Jessen, D. M. A. Mackenzie, K. Watanabe, T. Taniguchi, P. Bøggild, and T. J. Booth, Suppression of intrinsic roughness in encapsulated graphene, Phys. Rev. B **96**, 014101 (2017).

[26] D. A. Kirilenko, A. T. Dideykin, and G. Van Tendeloo, Measuring the corrugation amplitude of suspended and supported graphene, Phys. Rev. B **84**, 235417 (2011).

[27] R. Decker, Y. Wang, V. W. Brar, W. Regan, H.-Z. Tsai, Q. Wu, W. Gannett, A. Zettl, and M. F. Crommie, Local electronic properties of graphene on a BN substrate via scanning tunneling microscopy, Nano Lett. **11**, 2291 (2011).

[28] R. Pisoni, A. Kormányos, M. Brooks, Z. Lei, P. Back, M. Eich, H. Overweg, Y. Lee, P. Rickhaus, K. Watanabe, T. Taniguchi, A. Imamoglu, G. Burkard, T. Ihn, and K. Ensslin, Interactions and Magnetotransport through Spin-Valley Coupled Landau Levels in Monolayer MoS_2, Phys. Rev. Lett. **121**, 247701 (2018).

[29] J. Wierzbowski, J. Klein, F. Sigger, C. Straubinger, M. Kremser, T. Taniguchi, K. Watanabe, U. Wurstbauer, A. W. Holleitner, M. Kaniber, K. Müller, and J. J. Finley, Direct exciton emission from atomically thin transition metal dichalcogenide heterostructures near the lifetime limit, Sci. Rep. **7**, 12383 (2017).

[30] O. A. Ajayi, J. V. Ardelean, G. D. Shepard, J. Wang, A. Antony, T. Taniguchi, K. Watanabe, T. F. Heinz, S. Strauf, X.-Y. Zhu, and J. C. Hone, Approaching the intrinsic photoluminescence linewidth in transition metal dichalcogenide monolayers, 2D Mater. **4**, 031011 (2017).

[31] S. Shree, I. Paradisanos, X. Marie, C. Robert, and B. Urbaszek, Guide to optical spectroscopy of layered semiconductors, Nat. Rev. Phys. **3**, 39 (2021).

[32] S. Pezzini, V. Mišeikis, S. Pace, F. Rossella, K. Watanabe, T. Taniguchi, and C. Coletti, High-quality electrical transport using scalable CVD graphene, 2D Mater. **7**, 041003 (2020).

[33] J. E. Barrios-Vargas, B. Mortazavi, A. W. Cummings, R. Martinez-Gordillo, M. Pruneda, L. Colombo, T. Rabczuk, and S. Roche, Electrical and thermal transport in coplanar polycrystalline graphene-hBN heterostructures, Nano Lett. **17**, 1660 (2017).

[34] J. Vallejo Bustamante, N. J. Wu, C. Fermon, M. Pannetier-Lecoeur, T. Wakamura, K. Watanabe, T. Taniguchi, T. Pellegrin, A. Bernard, S. Daddinounou, V. Bouchiat, S. Guéron, M. Ferrier, G. Montambaux, and H. Bouchiat, Detection of graphene's divergent orbital diamagnetism at the Dirac point, Science **374**, 1399 (2021).

[35] A. Zugarramurdi, M. Debiossac, P. Lunca-Popa, A. J. Mayne, A. Momeni, A. G. Borisov, Z. Mu, P. Roncin, and H. Khemliche, Determination of the geometric corrugation of graphene on SiC(0001) by grazing incidence fast atom diffraction, Appl. Phys. Lett. **106**, 101902 (2015).

[36] H. Yang, A. J. Mayne, M. Boucherit, G. Comtet, G. Dujardin, and Y. Kuk, Quantum interference channeling at graphene edges, Nano Lett. **10**, 943 (2010).

[37] S. Haigh, A. Gholinia, R. Jalil, S. Romani, L. Britnell, D. Elias, K. Novoselov, L. Ponomarenko, A. Geim, and R. Gorbachev, Cross-sectional imaging of individual layers and buried interfaces of graphene-based heterostructures and superlattices, Nat. Mater. **11**, 764 (2012).

[38] F. J. García de Abajo, Optical excitations in electron microscopy, Rev. Mod. Phys. **82**, 209 (2010).

[39] M. Kociak and L. F. Zagonel, Cathodoluminescence in the scanning transmission electron microscope, Ultramicroscopy **176**, 112 (2017).

[40] A. Polman, M. Kociak, and F. J. G. de Abajo, Electron-beam spectroscopy for nanophotonics, Nat. Mater. **18**, 1158 (2019).

[41] L. H. G. Tizei, Y.-C. Lin, M. Mukai, H. Sawada, A.-Y. Lu, L.-J. Li, K. Kimoto, and K. Suenaga, Exciton Mapping at Subwavelength Scales in Two-Dimensional Materials, Phys. Rev. Lett. **114**, 107601 (2015).

[42] L. H. G. Tizei, Y.-C. Lin, A.-Y. Lu, L.-J. Li, and K. Suenaga, Electron energy loss spectroscopy of excitons in two-dimensional-semiconductors as a function of temperature, Appl. Phys. Lett. **108**, 163107 (2016).

[43] H. C. Nerl, K. T. Winther, F. S. Hage, K. S. Thygesen, L. Houben, C. Backes, J. N. Coleman, Q. M. Ramasse, and V. Nicolosi, Probing the local nature of excitons and plasmons in few-layer $\mathrm{MoS_2}$, npj 2D Mater. Appl. **1**, 2 (2017).

[44] P. K. Gogoi, Y.-C. Lin, R. Senga, H.-P. Komsa, S. L. Wong, D. Chi, A. V. Krasheninnikov, L.-J. Li, M. B. Breese, S. J. Pennycook *et al.*, Layer rotation-angle-dependent excitonic absorption in van der Waals heterostructures revealed by electron energy loss spectroscopy, ACS Nano **13**, 9541 (2019).

[45] E. Moynihan, S. Rost, E. O'Connell, Q. Ramasse, C. Friedrich, and U. Bangert, Plasmons in $\mathrm{MoS_2}$ studied via experimental and theoretical correlation of energy loss spectra, J. Microsc. **279**, 256 (2020).

[46] J. Hong, M. Koshino, R. Senga, T. Pichler, H. Xu, and K. Suenaga, Deciphering the intense postgap absorptions of monolayer transition metal dichalcogenides, ACS Nano **15**, 7783 (2021).

[47] S. Susarla, L. M. Sassi, A. Zobelli, S. Y. Woo, L. H. Tizei, O. Stéphan, and P. M. Ajayan, Mapping modified electronic levels in the moiré patterns in $\mathrm{MoS_2/WSe_2}$ using low-loss EELS, Nano Lett. **21**, 4071 (2021).

[48] A. Arora, N. K. Wessling, T. Deilmann, T. Reichenauer, P. Steeger, P. Kossacki, M. Potemski, S. Michaelis de Vasconcellos, M. Rohlfing, and R. Bratschitsch, Dark trions govern the temperature-dependent optical absorption and emission of doped atomically thin semiconductors, Phys. Rev. B **101**, 241413 (2020).

[49] D. Pommier, R. Bretel, L. E. P. López, F. Fabre, A. Mayne, E. Boer-Duchemin, G. Dujardin, G. Schull, S. Berciaud, and E. Le Moal, Scanning Tunneling Microscope-Induced Excitonic Luminescence of a Two-Dimensional Semiconductor, Phys. Rev. Lett. **123**, 027402 (2019).

[50] A. Castellanos-Gomez, M. Buscema, R. Molenaar, V. Singh, L. Janssen, H. S. J. van der Zant, and G. A. Steele, Deterministic transfer of two-dimensional materials by all-dry viscoelastic stamping, 2D Mater. **1**, 011002 (2014).

[51] D. G. Purdie, N. M. Pugno, T. Taniguchi, K. Watanabe, A. C. Ferrari, and A. Lombardo, Cleaning interfaces in layered materials heterostructures, Nat. Commun. **9**, 5387 (2018).

[52] See Supplemental Material at http://link.aps.org/supplemental/10.1103/PhysRevMaterials.6.074005 for more information on sample preparation, electron diffraction simulations, and roughness estimation.

[53] D. Y. Qiu, F. H. da Jornada, and S. G. Louie, Optical spectrum of $\mathrm{MoS_2}$: Many-Body Effects and Diversity of Exciton States, Phys. Rev. Lett. **111**, 216805 (2013).

[54] A. Arora, T. Deilmann, T. Reichenauer, J. Kern, S. Michaelis de Vasconcellos, M. Rohlfing, and R. Bratschitsch, Excited-State Trions in Monolayer $\mathrm{WS_2}$, Phys. Rev. Lett. **123**, 167401 (2019).

[55] K. Momma and F. Izumi, VESTA 3 for three-dimensional visualization of crystal, volumetric and morphology data, J. Appl. Crystallogr. **44**, 1272 (2011).

[56] D. B. Williams and C. B. Carter, Inelastic scattering and beam damage, in *Transmission Electron Microscopy* (Springer, 2009), pp. 53–71.

[57] C. T. Koch, Determination of core structure periodicity and point defect density along dislocations, Ph.D. thesis, Arizona State University, 2002.

[58] C. R. Dean, A. F. Young, I. Meric, C. Lee, L. Wang, S. Sorgenfrei, K. Watanabe, T. Taniguchi, P. Kim, K. L. Shepard, and J. Hone, Boron nitride substrates for high-quality graphene electronics, Nat. Nanotechnol. **5**, 722 (2010).

[59] L. Wang, Z. Chen, C. R. Dean, T. Taniguchi, K. Watanabe, L. E. Brus, and J. Hone, Negligible environmental sensitivity of graphene in a hexagonal boron nitride/graphene/h-BN sandwich structure, ACS Nano **6**, 9314 (2012).

[60] M. A. Stolyarov, G. Liu, S. L. Rumyantsev, M. Shur, and A. A. Balandin, Suppression of $1/f$ noise in near-ballistic h-BN-graphene-h-BN heterostructure field-effect transistors, Appl. Phys. Lett. **107**, 023106 (2015).

[61] L. H. G. Tizei, H. Lourenço-Martins, P. Das, S. Y. Woo, L. Scarabelli, C. Hanske, L. M. Liz-Marzán, K. Watanabe, T. Taniguchi, and M. Kociak, Monolayer and thin h-BN as substrates for electron spectro-microscopy analysis of plasmonic nanoparticles, Appl. Phys. Lett. **113**, 231108 (2018).

[62] Y. Y. Illarionov, G. Rzepa, M. Waltl, T. Knobloch, A. Grill, M. M. Furchi, T. Mueller, and T. Grasser, The role of charge trapping in $\mathrm{MoS_2/SiO_2}$ and $\mathrm{MoS_2}$ /hBN field-effect transistors, 2D Mater. **3**, 035004 (2016).

[63] C. Lee, S. Rathi, M. A. Khan, D. Lim, Y. Kim, S. J. Yun, D.-H. Youn, K. Watanabe, T. Taniguchi, and G.-H. Kim, Comparison of trapped charges and hysteresis behavior in hBN encapsulated single $\mathrm{MoS_2}$ flake based field effect transistors on $\mathrm{SiO_2}$ and hBN substrates, Nanotechnology **29**, 335202 (2018).

[64] H. Kohl and L. Reimer, *Transmission Electron Microscopy* (Springer, 2008).

[65] J. C. Meyer, F. Eder, S. Kurasch, V. Skakalova, J. Kotakoski, H. J. Park, S. Roth, A. Chuvilin, S. Eyhusen, G. Benner, A. V. Krasheninnikov, and U. Kaiser, Accurate Measurement of Electron Beam Induced Displacement Cross Sections for Single-Layer Graphene, Phys. Rev. Lett. **108**, 196102 (2012).

[66] A. I. C. Mihaila, T. Susi, and J. Kotakoski, Influence of temperature on the displacement threshold energy in graphene, Sci. Rep. **9**, 12981 (2019).

[67] S. Kretschmer, T. Lehnert, U. Kaiser, and A. V. Krasheninnikov, Formation of defects in two-dimensional $\mathrm{MoS_2}$ in the transmission electron microscope at electron energies below the knock-on threshold: The role of electronic excitations, Nano Lett. **20**, 2865 (2020).

[68] B. W. Smith and D. E. Luzzi, Electron irradiation effects in single wall carbon nanotubes, J. Appl. Phys. **90**, 3509 (2001).

[69] J. Kotakoski, D. Santos-Cottin, and A. V. Krasheninnikov, Stability of graphene edges under electron beam: Equilibrium energetics versus dynamic effects, ACS Nano **6**, 671 (2012).

[70] M. K. L. Man, S. Deckoff-Jones, A. Winchester, G. Shi, G. Gupta, A. D. Mohite, S. Kar, E. Kioupakis, S. Talapatra, and K. M. Dani, Protecting the properties of monolayer $\mathrm{MoS_2}$ on silicon based substrates with an atomically thin buffer, Sci. Rep. **6**, 20890 (2016).